

Optical tomographic image reconstruction from ultrafast time-sliced transmission measurements

W. Cai, S. K. Gayen, M. Xu, M. Zevallos, M. Alrubaiee, M. Lax, and R. R. Alfano

Optical imaging and localization of objects inside a highly scattering medium, such as a tumor in the breast, is a challenging problem with many practical applications. Conventional imaging methods generally provide only two-dimensional (2-D) images of limited spatial resolution with little diagnostic ability. Here we present an inversion algorithm that uses time-resolved transillumination measurements in the form of a sequence of picosecond-duration intensity patterns of transmitted ultrashort light pulses to reconstruct three-dimensional (3-D) images of an absorbing object located inside a slab of a highly scattering medium. The experimental arrangement used a 3-mm-diameter collimated beam of 800-nm, 150-fs, 1-kHz repetition rate light pulses from a Ti:sapphire laser and amplifier system to illuminate one side of the slab sample. An ultrafast gated intensified camera system that provides a minimum FWHM gate width of 80 ps recorded the 2-D intensity patterns of the light transmitted through the opposite side of the slab. The gate position was varied in steps of 100 ps over a 5-ns range to obtain a sequence of 2-D transmitted light intensity patterns of both less-scattered and multiple-scattered light for image reconstruction. The inversion algorithm is based on the diffusion approximation of the radiative transfer theory for photon transport in a turbid medium. It uses a Green's function perturbative approach under the Rytov approximation and combines a 2-D matrix inversion with a one-dimensional Fourier-transform inversion to achieve speedy 3-D image reconstruction. In addition to the lateral position, the method provides information about the axial position of the object as well, whereas the 2-D reconstruction methods yield only lateral position. © 1999 Optical Society of America

OCIS codes: 100.3190, 170.3010, 170.3880, 170.6920, 290.7050.

1. Introduction

The past decade has witnessed a rapid growth of research activities in optical imaging of objects located inside turbid media.¹⁻¹² This interest derives from potential practical applications of optical imaging in such diverse areas as detection of tumors in the human body, monitoring of aerosols and hydrometers in the atmosphere, and tracking of fuel droplets in the front nozzle of jet engines. Among these areas, biomedical applications have attracted the most attention because safe, noninvasive, and affordable imaging modalities with diagnostic ability can be developed using near-infrared light.² An intensely

pursued area is optical mammography in which near-infrared light is used to screen for breast cancer, a major and increasing health problem that affects one out of every eight women in the United States.¹³ X-ray mammography, the most commonly used breast imaging modality, is not suitable for imaging young dense breasts, may not distinguish between malignant and benign tumors, and frequent exposure to ionizing x rays could be harmful if used for routine screening. The impetus for developing optical mammography is to overcome some of these limitations of x-ray mammography and to achieve diagnostic ability by exploiting potential spectroscopic differences^{14,15} between the tumor and the surrounding tissues.

In its simplest form, optical imaging involves illuminating an object with light of appropriate wavelength and looking for its shadow in the transmitted light. Some difference in optical properties between the object and the surrounding medium is necessary for the formation of a shadow image. However, strong scattering of light by biological tissues severely degrades the image quality, and for sufficiently thick tissues, completely buries it in the background noise. Time-

The authors are with the Institute for Ultrafast Spectroscopy and Lasers, New York State Center of Advanced Technology for Ultrafast Photonic Materials and Applications, Departments of Physics and Electrical Engineering, The City College and Graduate Center of City University of New York, New York, New York 10031.

Received 12 November 1998; revised manuscript received 11 March 1999.

0003-6935/99/194237-10\$15.00/0
© 1999 Optical Society of America

resolved,^{3,5,6,11,12} and continuous-wave (cw)^{7,8} methods have been developed to sort out image-bearing ballistic and snake photons from the image-blurring multiple-scattered photons.¹⁶ These methods improve the image quality to different extents, but suffer from low signal-to-noise ratio when used for imaging through thick, highly scattering samples. Inverse image reconstruction (IIR) methods make use of the measured scattered light intensity around the object, knowledge (or estimate) of optical properties of the turbid medium and the object inside it, and mathematical models to construct images of the object.^{4,9,12,17–24} An IIR method requires extensive measurement of light intensities around the object and a long computation time for obtaining an image. Continuous-wave or frequency-modulated light, as well as ultrashort light, pulses may be used to accumulate data for IIR.

In this paper we report on a novel IIR approach that makes use of experimentally measured time-sliced two-dimensional (2-D) transmitted light intensity distribution, $I(x, y, t_i)$, to reconstruct three-dimensional (3-D) images. Time-sliced imaging is an extension of the idea of time-resolved early-light imaging except that picoseconds-duration temporal slices of the transmitted light covering both early-arriving less-scattered and late-arriving multiple-scattered photons are used to obtain a sequence of 2-D intensity patterns $I(x, y, t_i)$. Transmission measurements are carried out using a gated image intensifier that provides an approximately 80-ps duration time gate whose temporal position can be varied over a 20-ns range to collect a sequence of 2-D transmitted light intensity distribution $I(x, y, t_i)$. The inversion algorithm uses a 2-D matrix inversion with a one-dimensional (1-D) Fourier-transform inversion based on symmetry in cylindrical coordinates that greatly reduces computation time compared with direct 3-D inversion.

Our approach is a significant advance in optical tomographic imaging of turbid media. First, use of time-resolved data enables reconstruction of 3-D images that provide considerable information about object location in three dimensions. Depth information may not be available from direct transillumination methods, or even x-ray mammography that yields only 2-D images. It has been demonstrated recently that IIR approaches using cw measurements may not be adequate for a unique reconstruction of the internal optical characteristics of a scattering medium even when multiple sources and detectors are used.²⁵ Shifting of the positions of the source detector pairs may lead to 3-D image information, but it would make data acquisition highly time-consuming. Second, time-sliced data provide a wealth of information over a broad frequency range that is essential for 3-D image reconstruction as compared with frequency-domain schemes that commonly use several discrete frequencies. Frequency-domain methods may, in principle, scan over a broad continuous range of frequencies to generate data that are equivalent to time-domain methods. However, accumulation and processing of data over such a broad frequency range (several gigahertz) would be extremely time-consuming. More-

over, currently available sources cannot provide adequate power at such high frequencies. Use of time-resolved measurements is an effective way to collect data with adequate information content for 3-D image reconstruction.¹⁸ Another advantage of the present scheme that makes use of time-sliced 2-D light intensity patterns over earlier time-domain IIR schemes^{17,18} is speedy data acquisition. Those earlier schemes involving measurement of time-resolved profiles using multiple fibers and single-element detectors were time-consuming, expensive, and required complicated synchronization schemes. In the present scheme using a gated charge-coupled device (CCD) camera for detection, each pixel of the 384×288 pixels sensing element can be considered to be equivalent to a detector in the multidetector configuration mentioned above, and a 2-D spatial distribution of transmitted light intensity is obtained in every frame recorded by the camera. Use of only the transmitted light measured with a single CCD camera makes data acquisition simpler and faster than data acquisition that requires measurements of light intensity around the object using multiple detectors. Finally, use of a 2-D matrix inversion with a 1-D Fourier-transform inversion in the algorithm, together with fast time-gated data acquisition, enables reconstruction of 3-D images within a short time, a key requirement for real-time clinical applications. Although the linear perturbative approach has been used before, this use of a 2-D matrix inversion with a 1-D Fourier-transform inversion for speedy image reconstruction is a new salient feature of our approach.

As a proof of concept, we used the method to reconstruct images of an absorbing object placed inside a tissue-simulating model turbid medium. We obtain good localization of the object in the lateral dimensions. Spatial resolution along the axial direction is promising, but needs improvement. The remainder of this paper is organized as follows. Section 2 details the experimental arrangement, sample characteristics, and data-acquisition scheme. The IIR algorithm is presented in Subsection 3.A. Because the inversion problem is ill-posed, some form of regularization is needed to extract useful image information. The degree of regularization is typically controlled by parameters that are usually chosen empirically. The L -curve method²⁶ that we use to select optimal regularization parameters is described in Subsection 3.B. The formalism is used to reconstruct images of an absorbing object inside a turbid medium and the results are presented in Section 4. The results of reconstruction using simulated data presented in Subsection 4.A is compared with that obtained using experimental data presented in Subsection 4.B. Implications of these results for obtaining tomographic images of biological tissues and the scope of this IIR approach are discussed in Section 5.

2. Experimental Method and Materials

The experimental arrangement for picosecond-duration time-sliced measurement of transmitted light intensity is displayed schematically in Fig. 1(a).

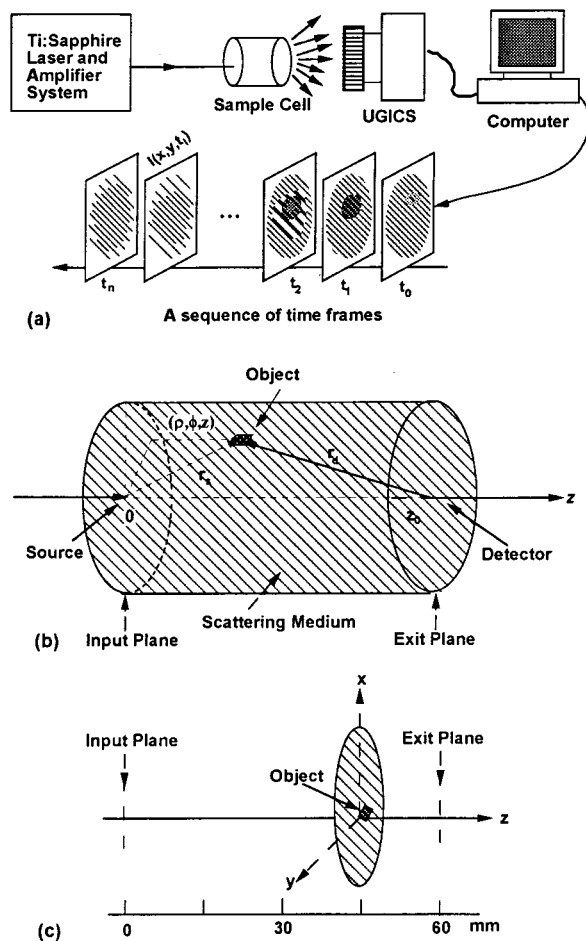


Fig. 1. (a) Schematic diagram of the experimental arrangement used for time-sliced transmitted intensity measurements. (b) Geometric arrangement used to describe the reconstruction algorithm showing the object and image planes and the object in an arbitrary position in cylindrical coordinates. (c) Object location in a lateral plane parallel to and 15 mm away from the exit plane. The 10-mm side of the sample was inclined at an angle of approximately 15° with the vertical (x axis). This is the object position that was used in the experiment.

The detail of the cylindrical sample cell geometry is presented in Fig. 1(b). The location of the object on a plane parallel to and 15 mm toward the source from the exit plane (45 mm from the input plane) is shown in Fig. 1(c). The scattering medium was a suspension of Intralipid-10% (Kabi Pharmacia Inc., Clayton, North Carolina) in water. Intralipid-10% is a fat emulsion used clinically as a nutrient and in research as a phantom to investigate light propagation in tissues. The concentration of Intralipid-10% suspension was adjusted to provide an estimated reduced scattering coefficient μ_s' of 0.4 mm^{-1} and an absorption coefficient μ_a of 0.02 mm^{-1} at 800 nm.²⁷ The Intralipid suspension was held in a 60-mm-long and 200-mm-diameter cylindrical Plexiglas cell. The cell thickness was chosen to be equivalent to that of an average breast under the extent of compression commonly used in x-ray mammography.

The object to be imaged was a $3 \times 3 \times 10 \text{ mm}^3$ rectangular parallelepiped made of aluminum and painted black. It was suspended on axis at a distance of 15 mm ($z = 45 \text{ mm}$) from the exit plane and absorbed most of the light incident on it. The cell was illuminated through the input plane with 150-fs duration, 1-kHz repetition rate pulses of 800-nm light from a Ti:sapphire laser and amplifier system.²⁸ The 3-mm-diameter collimated laser beam with an average power of approximately 100 mW was incident along the axis (z axis) onto one of the flat faces (input plane) of the cylindrical cell.

The 2-D intensity distribution of light emergent from the opposite endface of the cell (exit plane) was collected by a 24-mm focal-length $f/2.8$ camera lens with a 84° angle of view and was recorded by the ultrafast gated intensified camera system (UGICS). The UGICS is a compact gated image intensifier unit that is fiber optically coupled to a CCD camera. It provides an electronic time gate whose FWHM duration could be adjusted to a minimum of approximately 80 ps. The gate position could be varied over a 20-ns range with a minimum step size of 25 ps. The signal recorded by the system at a particular gate position is a convolution of the transmitted light pulse with the gate pulse centered on the gate position. The collection optics was adjusted to capture light transmitted through the exit plane, and no attempt was made to use the scattered light emergent through the curved surface of the cell. The data then consisted of a sequence of time-resolved 2-D intensity distribution integrated over the gate duration at different gate positions, $I(x, y, t_i)$. Because $I(x, y, t_i)$ is the 2-D spatial intensity distribution integrated over a 80-ps slice of time for the gate position t_i , we refer to it as a time-sliced intensity pattern (or intensity distribution). These time-sliced intensity patterns were recorded by the CCD camera and displayed on a personal computer.

In the experiment reported here, the gate width was adjusted to 80 ps and $I(x, y, t_i)$ were recorded over a 5-ns range by varying the gate pulse position in steps of 100 ps. The zero time was taken to be the instant when the incident light pulse entered the front surface of the cell. $I(x, y, t_i)$ provided the experimental data for IIR.

Experimentally recorded typical 2-D intensity patterns of transmitted light with the object inside the medium are shown in Figs. 2(a) and 2(b) for gate positions of 700 ps and 1500 ps, respectively. The 1500-ps pattern is spatially more spread out than the 700-ps pattern because the electronic time gate collects light that is more diffuse and hence spatially spread out at the 1500-ps position than that at the 700-ps position. Intensity patterns recorded with later gate positions spread out even further. Because the temporal profile of the transmitted light intensity peaks around 2 ns, the intensity at the center of the 1500-ps pattern is higher than that of the 700-ps pattern. No shadow image of the object was apparent in either of the intensity patterns. All the intensity patterns measured over the 5-ns range were

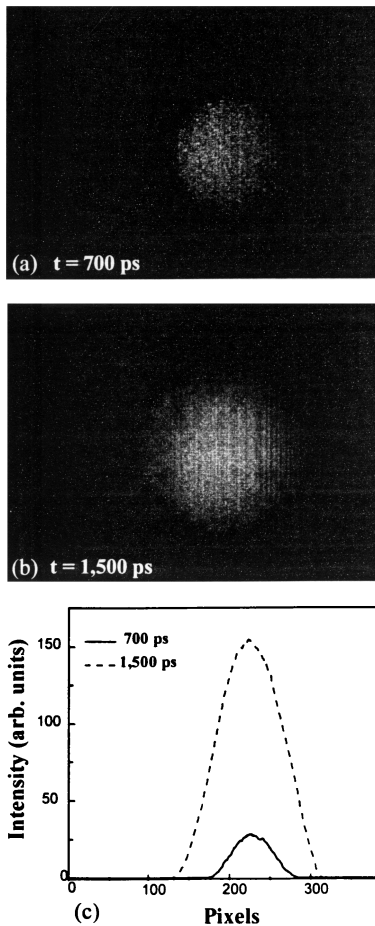


Fig. 2. Experimentally measured 2-D intensity distribution of light transmitted through the scattering medium with the object for a gate position of (a) 700 ps and (b) 1500 ps. (c) The object was located approximately on the axis of the cylindrical cell at a distance of 15 mm from the exit plane.

transferred to a Silicon Graphics Origin-2000 computer for use as experimental data for 3-D IIR. The computer has four parallel 195-MHz CPU's, but only one was used in this research.

3. Reconstruction Formalism

A. Algorithm

The time-sliced IIR formalism presented here is based on the diffusion approximation of the radiative transport theory for photon migration in a scattering medium.⁹ The diffusion equation in a turbid medium is given by

$$\left\{ \frac{\partial}{\partial t} + \mu_a(\mathbf{r})c - \nabla[D(\mathbf{r})c\nabla] \right\} I(\mathbf{r}, t) = S(\mathbf{r}, t), \quad (1)$$

where I is the photon density (photons/cm³), S is the source strength [photons/(cm³·s)], μ_a is the absorption coefficient, $D = 1/\{3[\mu_a + (1 - g)\mu_s]\}$ is the diffusion coefficient, μ_s is the scattering coefficient, g is the scattering anisotropy factor, and c is the speed of light in the medium. We are interested in the

following problem: Given the time-sliced intensity pattern transmitted through the media with the object $I(x, y, t_i)$, and without the object $I_0(x, y, t_i)$, we want to reconstruct a map of the change in optical parameters, the absorption coefficient in this case. The medium without the object is referred to as the reference medium.

The formulation of the forward problem uses a slab geometry $(0, z_0)$ formed by cylindrical coordinates (ρ, φ, z) , as shown schematically in Fig. 1(b). A point source (or a φ -symmetric finite source) is assumed to be located (or is centered) at $(0, 0, 0)$. The detector system is located on the z_0 plane and is mapped onto the CCD camera by a lens. The ρ boundary is assumed to be at infinity. However, it can be replaced by a finite boundary using a more complex Green's function. We use a Green's function perturbative approach under the Rytov approximation^{4,29} to produce a linear inverse algorithm.^{9,17} The Rytov approximation is used because it has been shown to provide a more accurate reconstruction of the absorptive properties than the Born approximation.²⁹ The reference medium, i.e., the medium without the object, is assumed to be uniform. Our formulation requires only the surrounding medium and not the object to be cylindrically symmetric, a condition that can be arranged in an experiment. For example, in the case of breast imaging the breast may be placed in a cylindrical cell containing an index-matching liquid with optical properties that are similar to the average values of optical properties of a real breast. The aim of the reconstruction process would then be to obtain a spatial map of the difference in optical properties from those average values. Thus the assumption of cylindrical symmetry for the surrounding medium is not a serious limitation for the applicability of the formalism.

The forward problem can be represented in matrix form as

$$\mathbf{Y} = \mathbf{W}\mathbf{X}, \quad (2)$$

where \mathbf{Y} is a vector represented by a column matrix whose elements are measured changes in transmitted intensity, \mathbf{X} is a vector whose elements are optical parameter (absorption or scattering coefficient) changes that are due to the presence of the object, and \mathbf{W} is the weight function,⁹ which, in the linear inversion case, is related only to the reference medium. The vector \mathbf{Y} has M elements, determined from the experimental data as $Y_i = -\log(I_i/I_{oi})$, where I_i and I_{oi} are the measured intensities with and without the object, respectively, and $M = (n_t \times n_r \times n_\phi)$ where n_t is the number of time slices and n_r and n_ϕ are the numbers of radial and angular sections, respectively, that the detector plane is divided into. \mathbf{X} has N elements, $X_j = c\Delta\mu_a(\mathbf{r}_j)$ or $c\Delta D(\mathbf{r}_j)$, where N is the number of voxels that the sample cell is divided into. \mathbf{W} is an $M \times N$ matrix that, under the assumptions of a cylindrical boundary and a uniform reference medium, satisfies the φ -rotation invariance, i.e., it is a function of $\varphi - \varphi_d$, where φ_d is the angle coordinate of

a point on the detector plane and φ is the angle coordinate of a voxel. It should be pointed out that the reference medium (not the object) needs to be cylindrically symmetric. For time-resolved absorption tomography, W is written as

$$W_{3-D}(\rho_d, \rho, z, \varphi - \varphi_d t) = \frac{\Delta V}{G_\rho^0(\rho_d, t)G_z^0(z_0, 0, t)} \times \int_0^t d\tau \frac{1}{4\pi Dc(t - \tau)} \times \exp\left[\frac{-\rho^2 - \rho_d^2 + 2\rho\rho_d \cos(\varphi - \varphi_d)}{4Dc(t - \tau)}\right] \times G_z^0(z, z_0, t - \tau)G_\rho^0(\rho, \tau)G_z^0(z, 0, \tau). \quad (3)$$

In Eq. (3), $G_z^0(z, 0, t)$ is a 1-D slab Green's function for the reference medium with source at $z = 0$ and is written as

$$G_z^0(z, 0, t) = (4\pi Dct)^{-1/2} \exp(-z^2/4Dct) + \sum_i (4\pi Dct)^{-1/2} \exp[-(z - z_i)^2/4Dct],$$

where i denotes the i th image source that is due to the slab geometry.

$G_\rho^0(\rho, t)$ is a 2-D Green's function with the source located (or centered) at $\rho = 0$. For a point source, it is of the form

$$G_\rho^0(\rho, t) = \frac{1}{4\pi Dct} \exp\left(\frac{-\rho^2}{4Dct}\right), \quad (4)$$

and for a finite-size spot source, it is written as

$$G_\rho^0(\rho, t) = \frac{1}{2Dct} \int f(\rho_s) \exp\left(-\frac{\rho^2 + \rho_s^2}{4Dct}\right) I_0\left(\frac{2\rho\rho_s}{4Dct}\right) \rho_s d\rho_s, \quad (5)$$

where I_0 is the zeroth-order modified Bessel function and $f(\rho_s)$ is the intensity distribution of the incident light spot.

After making a 1-D Fourier transform of W_{3-D} over $\varphi - \varphi_d$, we obtain K -independent 2-D matrices, $W_{2-D}(k)$ parameterized by k , with K the number of grid points in the Fourier k space. The indices of $\varphi - \varphi_d$ in the 3-D real space correspond to indices of k in the Fourier space. $W_{2-D}(k)$ is an $M' \times N'$ matrix, with $M' = (\text{number of } \rho_d \text{ division}) \times (\text{number of time slices})$, and $N' = (\text{number of } \rho \text{ division}) \times (\text{number of } z \text{ division})$. The normal form $W_{2-D}(k)^T W_{2-D}(k)$ is an $N' \times N'$ matrix. We separately calculate the K inverse matrices $[W_{2-D}(k)^T W_{2-D}(k) + \Lambda(k)]^{-1}$, $k = 1, 2, \dots, K$, where $\Lambda(k)$ is a matrix for regularization. The computational complexity now is K times that of inverting a W_{2-D} matrix, which is much less than that of inverting a W_{3-D} matrix.

Having experimental data $\mathbf{Y}(\rho_d, \varphi_d, t)$, we make a Fourier transform over φ_d to obtain $\mathbf{Y}(\rho_d, k, t)$, $k = 1, 2, \dots, K$. The technique for fast discrete Fourier

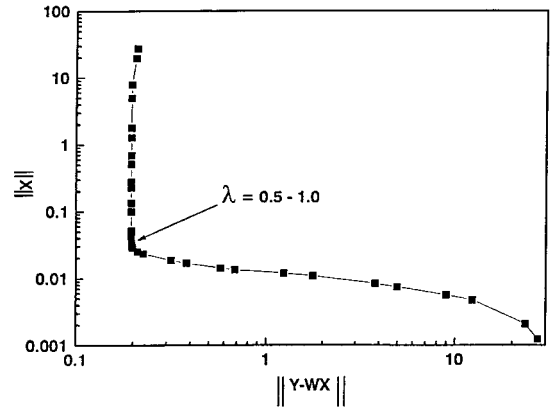


Fig. 3. L curve used for choosing the regularization parameters for IIR with simulated data. The object was located at a distance of 15 mm from the exit plane.

convolution is used. We then use simple matrix multiplication to obtain the image in the k space:

$$\mathbf{X}(k) = \mathbf{Y}(k)^T W_{2-D}(k) [W_{2-D}(k)^T W_{2-D}(k) + \Lambda(k)]^{-1}, \quad k = 1, 2, \dots, K. \quad (6)$$

After $\mathbf{X}(k)$, $k = 1, 2, \dots, K$, is obtained, the inverse 1-D Fourier transform over k reproduces the X as a function of φ and gives the 3-D distribution of the changes in absorption (or scattering) coefficients $\mathbf{X}(\rho, \varphi, z)$.

B. Regularization

The inversion problem is ill-posed with a huge condition number, hence a regularization procedure is necessary to obtain a unique solution. We use a diagonal form of a regularization matrix $\Lambda(k) = \lambda(k)\delta_{ij}$. A convenient way to understand the effect of regularization and to choose the suitable regularization parameter is to use the L curve,²⁶ which shows the properties of the regularized solution \mathbf{X}_λ that vary with λ . Two properties of the \mathbf{X}_λ are the norm $\|\mathbf{X}_\lambda\|$ and the norm of the corresponding residual vector $\|\mathbf{W}\mathbf{X}_\lambda - \mathbf{Y}\|$. $\|\mathbf{X}_\lambda\|$ indicates the stability of the solution and it decreases with an increase of λ . $\|\mathbf{W}\mathbf{X}_\lambda - \mathbf{Y}\|$ indicates the error that is due to the introduction of regularization and it increases with an increase of λ . As proved in Ref. 26, if $\|\mathbf{X}_\lambda\|$ versus $\|\mathbf{W}\mathbf{X}_\lambda - \mathbf{Y}\|$ is plotted with different values of λ , a curve similar in shape to the capital letter L is obtained. It suggests that a good regularization parameter is one that corresponds to a regularized solution near the corner of the L curve because in this region there is a good compromise that keeps both $\|\mathbf{X}_\lambda\|$ and $\|\mathbf{W}\mathbf{X}_\lambda - \mathbf{Y}\|$ relatively small. Figure 3 shows an L curve that we obtained for one of our simulation tests, which corresponded to $W_{2-D}(k = 1)$. The simulation assumed a Gaussian-distributed noise level with a root-mean-square deviation of 5% (for brevity henceforth referred to simply as 5% Gaussian noise) in each simulated value of Y . The range of the values of λ varies from 10^{-8} to 10^8 . The values of λ corresponding to positions near the corner of the L curve are approximately 0.5–1.0. Choice of a value of λ be-

tween 0.5–1.0 in our inversion calculation led to a stable image of the object with the 5% Gaussian noise.

4. Results

A. Three-Dimensional Image from Simulated Data

In the simulation, the thickness of the slab was taken to be $z_0 = 60$ mm. A point light source was assumed. The detector system was taken to be a circle with a radius $R_d = 30$ mm. To choose grids of equal area, the angle 2π was uniformly divided into 36 parts, whereas the radius R_d was divided into 30 parts scaled such that the outer radius of the j th disk was $R_j = (R_d^2 j/J)^{1/2}$, where $j = 1, 2, 3, \dots, J$, with $J = 30$. In each simulated temporal profile, intensities at 30 time slices uniformly distributed from 450 to 1900 ps were taken. The number of sampling data was $M = 30 \times 36 \times 30$. Data both with and without the object were used to obtain $Y_i = -\log(I_i/I_o)$, after adding the 5% Gaussian noise. The sample cell was divided into $N = 10 \times 36 \times 20$ voxels, with 20 divisions along the z direction and 10 divisions along the ρ direction in a 30-mm range in a way similar to that used for detector division.

Elements of W were calculated using Eq. (3) with a background-reduced scattering coefficient μ_s' of 0.4 mm^{-1} and an absorption coefficient μ_a of 0.02 mm^{-1} . Corresponding parameters of the object were $\mu_s' = 0.4 \text{ mm}^{-1}$ and $\mu_a = 0.4 \text{ mm}^{-1}$. The regularization parameter λ was taken to be 1.0 based on the L -curve analysis. Image of the absorbing object obtained using Eq. (6) and the 1-D Fourier transform is shown in Fig. 3. The 20 consecutive circles in Fig. 4 represent the images at 3-mm intervals along the cylinder axis (z axis) from the input plane to the exit plane. A gray scale is used to display the spatial distribution of changes in the absorption coefficient, with black representing the maximum value. For simulation the object of 3-mm linear dimension was placed in a voxel located in the 15th division along the z axis ($z = 45$ mm) that was approximately 15 mm away from the exit plane.

The reconstructed image locates the object in the neighborhood of where it was placed, as can be seen from the concentration of black around the 15th circle. The image [$\Delta\mu_a(\mathbf{r})$ distribution] appears to be spread out both in the lateral and in the axial directions, a consequence of the scattering and the diffusion approximation used for reconstruction. The FWHM of the image is approximately 6 mm in the lateral plane and approximately 12 mm in the axial direction.

B. Three-Dimensional Image from Experimental Data

In the IIR using experimental data, we approximated the laser beam to be a point source located at the center of the $z_0 = 0$ -mm plane. The ρ boundary of the container was assumed to be at infinity. The time-resolved 384×288 pixels image from the CCD camera, with and without the object, were transformed to provide $30 \times 36 \times 30$ pieces of \mathbf{Y} data, as

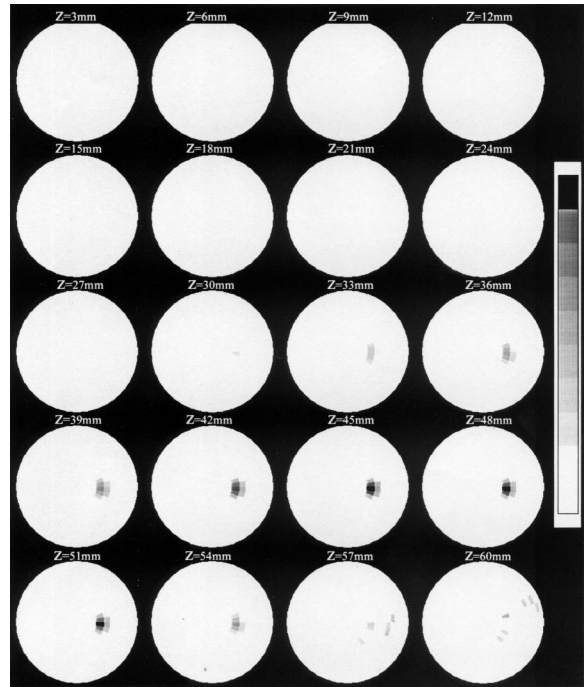


Fig. 4. Images reconstructed from simulated data when the object was located at a distance of 15 mm ($z = 45$ mm) from the exit plane. The sequence of circles represents images at 3-mm intervals along the cylinder axis. The linear intensity scale spans the range 0–20. The maximum value of $\Delta\mu_a(\mathbf{r})$ is 0.04 mm^{-1} and the size of the object is $3 \times 3 \times 3 \text{ mm}^3$.

was done in simulation. The plot of $\|\mathbf{X}_\lambda\|$ versus $\|\mathbf{W}\mathbf{X}_\lambda - \mathbf{Y}\|$ for computing the regularization parameter λ showed only a small kink on the curve instead of a clear L shape. The norm of the residual vector $\|\mathbf{W}\mathbf{X}_\lambda - \mathbf{Y}\|$ at kink position was approximately 2 orders of magnitude larger than that in the simulated case. This difference may be due to the deviation of the experimental conditions from the assumptions of the theoretical forward model or because of a higher noise level in the experiment than that used in the simulation. Based on our simulation results assuming higher noise levels, we believe that the difference between the simulated and the experimental results mainly comes from higher experimental noise. Possible sources of experimental noise are pulse-to-pulse energy fluctuation in the laser beam and timing jitter in the gate position. Because we arrange a small object at the distance far enough from the source and the detectors, use of the diffusion equation with the Rytov approximation seems reasonable. Figure 5 shows a 3-D image of the object as a sequence of frames at 3-mm intervals along the axial direction reconstructed using experimental data. The lateral position of the object is reconstructed to be near the cylinder axis in the image map, as one would expect. However, the image is spread out with a half-width of approximately 20 mm along the axial direction. The absorption coefficient distribution appears to be peaked more toward the detector end than the actual object position.

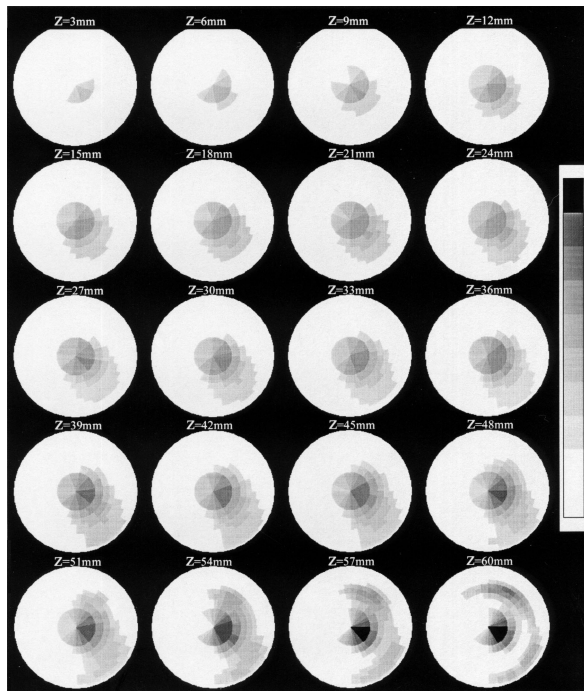


Fig. 5. Images reconstructed from experimental data with the object located at a distance of 15 mm ($z = 45$ mm) from the exit plane. The sequence of circles represents images at 3-mm intervals along the cylinder axis.

One of the edges of the object was placed on the axis for experimental simplicity only and should not be considered a limitation of the present IIR approach. Reconstruction using simulated data produced a stable solution even when the object was located closer to the cylinder boundary than to the cylinder axis.

5. Discussion

Results of this study indicate that the time-sliced transmission measurements along with the diffusion tomographic IIR method can provide a 3-D map of the location of the object inside a biological tissue-simulating turbid medium. A salient feature of the approach is how short a time it takes for inverse reconstruction. Our estimate shows that a 3-D image of $10 \times 36 \times 20$ voxels can be obtained with a running time of less than 1 min on a Silicon Graphics Origin-2000 computer when only one of its four parallel 195-MHz CPU's is used in the computation. The speed is comparable with that of a 200-MHz Pentium CPU. Combined with a fast data-acquisition scheme that we developed, this algorithm shows the potential for near-real-time IIR.

The reconstructed image of the object has the lateral position that one would expect from the experimental arrangement. The axial position is less certain, as the change in absorption coefficient $\Delta\mu_a(\mathbf{r})$ is more spread out in the axial direction. Comparison with image reconstructed from simulated data indicates that better axial localization is obtained using simulated data than that from the experiment. The position of the object in the reconstructed image

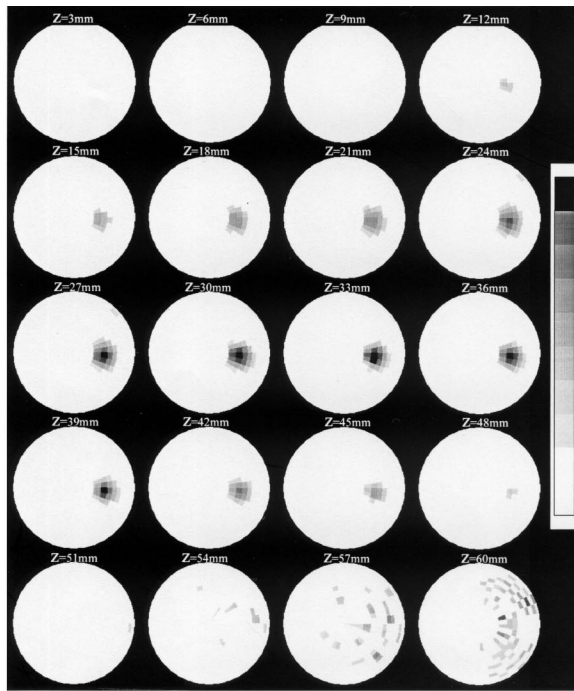
gets shifted toward the detector plane for both the simulated and the experimental data. The shift is more pronounced for the image reconstructed using experimental data.

To further investigate this apparent shift in the peak position and the extent of localization, we carried out inverse reconstruction with simulated data (a) for different axial positions of the object and (b) for different noise levels. Reconstructed images using simulated data with a 5% Gaussian noise level for object locations of 30 mm ($z = 30$ mm) and 45 mm ($z = 15$ mm) from the exit plane are shown in Figs. 6(a) and 6(b), respectively. Figures 6(a) and 6(b) along with Fig. 4 indicate that, as the object is moved further away from the detector end, its localization in the reconstructed images becomes poorer. The absorption coefficient change $\Delta\mu_a(\mathbf{r})$ spreads out both in the axial and in the lateral directions with a consequent decrease in its peak value as the object distance from the exit plane increases. The result is expected because the further away the object is from the exit plane the higher is the probability for the image-bearing light to spread out and multiply scattered light to encroach into the region of a geometric shadow cast by the absorbing object. The overall effect is a smearing out of the shadow image. The diffusion approximation-based model used here is sensitive to that spreading and reconstructs images whose size and sharpness depend on the object location.

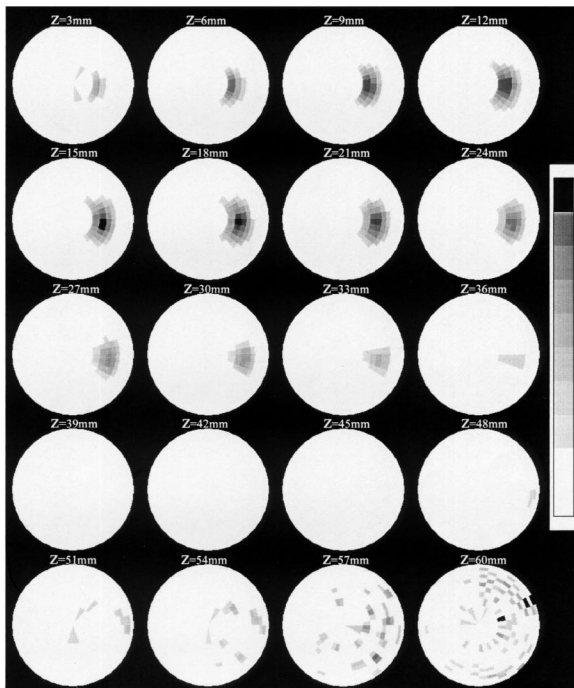
The shift in the peak position of reconstructed $\Delta\mu_a(\mathbf{r})$ distribution toward the exit plane was observed for all three positions of the object. A qualitative explanation for this shift can be given in terms of the dependence of imaging sensitivity on the object location. It is a common observation that for diffuse light imaging, if the object is located on the exit plane it is imaged with minimal distortion and optimal sharpness. Image sharpness decreases and distortion increases as the object is moved further into the scattering medium. Imaging sensitivity is then a function that peaks on the exit plane and gradually decreases toward the input plane. The $\Delta\mu_a(\mathbf{r})$ distribution in the reconstructed image would be proportional to a convolution of this function with $\Delta\mu_a(\mathbf{r})$ distribution of the object and would be shifted toward the exit plane.

The spreading out of the $\Delta\mu_a(\mathbf{r})$ distribution leads to a decrease in its amplitude in the reconstructed image as well because the magnitude of the inhomogeneity gets distributed over a larger region of space. For a small object in three dimensions, the spreading of its image can dramatically decrease the amplitude of imaged optical parameters, in this case $\Delta\mu_a(\mathbf{r})$. This accounts for the peak amplitude of 0.04 mm^{-1} in the reconstructed image of Fig. 4, although the input value of the inhomogeneity was 0.4 mm^{-1} .

Another consequence of the imaging sensitivity being peaked on the exit plane is the observed higher noise level in the $z = 60$ -mm frame (exit plane) of the reconstructed images of Figs. 4, 6(a), and 6(b). The noise in the exit plane seems to be more pronounced



(a)



(b)

Fig. 6. Images reconstructed from simulated data when the object was located at a distance of (a) 30 mm ($z = 30$ mm) and (b) 45 mm ($z = 15$ mm) from the exit plane. The sequence of circles represents images at 3-mm intervals along the cylinder axis.

as the object is moved toward the input plane, although the same 5% Gaussian noise level was used for all three cases. The apparent higher noise in Fig. 6(b) is a consequence of the way the $\Delta\mu_a(\mathbf{r})$ distribution is displayed in these figures. The ratio of peak

value of $\Delta\mu_a(\mathbf{r})$ to the magnitude of the noise level determines how prominently the noise will be displayed in the scheme used in Figs. 4, 6(a), and 6(b). Because of the object location of 45 mm from the exit plane, the peak value of $\Delta\mu_a(\mathbf{r})$ is much smaller than that of the other two cases, the noise level appears to be more pronounced in the $z = 60$ -mm frame of Fig. 6(b). Simulations with higher noise levels lend support to this observation. With a high enough input noise level, the noise in the exit plane could be as pronounced as the peak value of $\Delta\mu_a(\mathbf{r})$ in the image of the object.

The above observations of peak shift and exit plane noise with simulated data help explain the apparent lower localization and larger shift toward the detector plane of the image from experimental data shown in Fig. 5. We ascribe these to the above-mentioned peaking of imaging sensitivity toward the exit plane and the higher noise level in the experiment compared with the 5% used in simulation. Sources of noise could be energy fluctuation of pulses from the laser amplifier, long-term drift of the laser output, jitters in the position and width of the time gate, and the CCD dark noise. Ample room exists for improvement of the experimental noise and hence object localization. In this proof-of-the-principle experiment, our aim was to test if the algorithm provided meaningful 3-D images from time-sliced 2-D experimental data.

One way of reducing the magnitude of peak shift and improving the localization of the object in the reconstructed image would be to use two sets of data for reconstruction—one taken with the source and detector positioned as described in the text and the second with the z positions of the source and detector reversed. To test this concept, we carried out the reconstruction using the two sets of simulated data as mentioned above for the object position of Fig. 4, that is, 15 mm toward the source from the exit plane. The result, displayed in Fig. 7, shows improvement in object localization when compared with the image in Fig. 4. The improvement will be more substantial for an object located deeper into the scattering medium as a comparison of Fig. 7 with that of Fig. 6(b) reveals.

The IIR scheme presented above would be applicable to imaging of breast *in vivo*. The optical properties, transport parameters, and thickness of the scattering medium used in this experiment are not too far removed from that of breast tissues. Although measurement on the breast with the lesion would provide the signal I , the reference I_0 can be obtained by using a uniform phantom with optical parameters that are equivalent to the average value of the parameters for the breasts. Another interesting possibility is to use measurements using the light of two different but nearby wavelengths. If a wavelength that is resonant with the lesion can be determined, then measurements at that wavelength can be used as the signal and measurements with a non-resonant wavelength can be used as the reference. It should be noted that such lesion-specific wave-

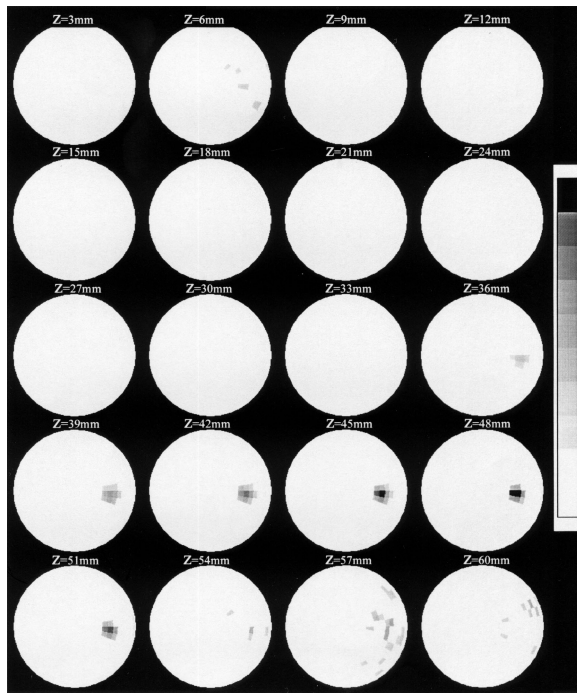


Fig. 7. Images reconstructed from simulated data when the object was located at a distance of 15 mm ($z = 45$ mm) from the exit plane. Image reconstruction was carried out with data collected using the direct arrangement of both the source and the detector, as well as reversing their positions in the z direction.

lengths are not well established yet. However, our spectroscopic imaging measurements indicate that if the imaging light is tuned into and out of the optical resonance of adipose breast tissues, then the adipose tissues could be highlighted in the transillumination image.³⁰ Combined spectroscopic and time-sliced measurements may provide much more information for tomographic image reconstruction than that available from single-wavelength x-ray mammography. Identification of fingerprint wavelengths for cancer diagnosis is an actively pursued area of current research. Imaging with such lesion-specific light, if identified, holds the promise for simultaneous detection, localization, and diagnosis of lesions, a unique potential advantage of optical mammography.

One criticism sometimes raised about use of a reference system is that measurements without the object in the reconstruction algorithm need to be addressed. Because our inverse algorithm is linear, the difference in the absorption coefficient between the object and the medium is relevant and the choice of a reference is arbitrary. In principle, it should be possible to reconstruct images from a set of time-sliced measurements on the object in the medium alone and take for the reference medium a uniform background characterized by the average values of optical properties. For example, in an optical mammography application, a uniform medium with values of the optical properties similar to the respective average values of optical properties in the real breast

could be considered a reference medium. The algorithm would try to estimate the difference between that assumed background distribution and measurement on the system with the object. The estimation can be carried out as long as the perturbation approach remains valid. Alternatively, only measurements on the object within the medium using two different but nearby wavelengths of light could be used for the signal and reference, as discussed above.

Our IIR method presents a linear approach based on the Rytov approximation, and we were particularly interested in small objects, i.e., weak perturbation. One of the practical reasons for choosing small objects is that breast tumors need to be detected at an early stage of development when they are small in size and are more treatable. Also, the difference in optical properties between normal and cancerous tissues are generally not too large. The magnitude of perturbation depends on the size of both the object and the amplitude of changes in the optical properties between the object and the surrounding medium. The combination is expected to be in the domain of small perturbation for early breast tumors. We considered small objects with high optical contrast that seemed to satisfy the requirements for the linear approach to hold as evident from the stable inverse solutions that we obtained. Linear approaches using frequency-domain measurements were shown to yield inverse images for extended objects by other groups.^{4,20,29} The present approach is expected to yield qualitatively adequate results for multiple objects, and extended objects in the strong perturbation limit as well, although the details of the object shape and amplitude of optical parameter changes may not be quantitatively precise. However, at the current state of development, similar limitations are shared by other linear and nonlinear approaches as well. The advantages of the present linear approach are speed of reconstruction, ability to provide 3-D images, and generation of stable solutions without the need for artificial termination of iteration to avoid divergence that is needed for nonlinear methods. Unlike nonlinear iterative methods,^{22,23} the linear approach is more susceptible to producing erroneous results for large and strong objects.

In summary, even with the above-mentioned caveats and present limitations, the wavelength-dependent, time-sliced transmission measurements and the diffusion tomographic inverse algorithm show promise for providing 3-D images of objects in a turbid medium, such as a tumor in a breast within a clinically acceptable time frame.

This research is supported in part by the National Aeronautics and Space Administration, the U.S. Army Medical and Materiel Research Command, the Mediscience Technology Corp., and the New York State Science and Technology Foundation.

References and Notes

1. For a brief review of optical imaging techniques, see S. K. Gayen and R. R. Alfano, "Emerging optical biomedical imaging techniques," *Opt. Photon. News* 7(3), 16–22 (1996).

2. G. J. Muller, R. R. Alfano, S. R. Arridge, J. Beuthan, E. Gratton, M. Kaschke, B. R. Masters, S. Svanberg, and P. van der Zeeet, eds., *Medical Optical Tomography: Functional Imaging and Monitoring*, Vol. IS 11 of SPIE Institute Series (SPIE, Bellingham, Wash., 1993).
3. L. Wang, P. P. Ho, C. Liu, G. Zhang, and R. R. Alfano, "Ballistic 2-D imaging through scattering wall using an ultrafast Kerr gate," *Science* **253**, 769–771 (1991).
4. M. A. O'Leary, D. A. Boas, B. Chance, and A. G. Yodh, "Experimental images of heterogeneous turbid media by frequency-domain diffusing-photon tomography," *Opt. Lett.* **20**, 426–428 (1995), and relevant references therein.
5. R. R. Alfano, X. Liang, L. Wang, and P. P. Ho, "Time-resolved imaging of translucent droplets in highly scattering turbid media," *Science* **264**, 1913–1915 (1994).
6. M. R. Hee, J. Izzat, J. Jacobson, J. G. Fujimoto, and E. A. Swanson, "Femtosecond transillumination optical coherence tomography," *Opt. Lett.* **18**, 950–952 (1993).
7. M. Cutler, "Transillumination as an aid in the diagnosis of breast lesion," *Surg. Gynecol. Obstet.* **48**, 721–730 (1929).
8. A. O. Wist, P. P. Fatouros, and S. L. Herr, "Increased spatial resolution in transillumination using collimated light," *IEEE Trans. Med. Imaging* **12**, 751–757 (1993).
9. S. R. Arridge, "The forward and inverse problems in time-resolved infrared imaging," in *Medical Optical Tomography: Functional Imaging and Monitoring*, Vol. IS 11 of SPIE Institute Series (SPIE, Bellingham, Wash., 1993).
10. E. Gratton, W. Mantolin, M. vande Ven, J. Fishkin, M. Maris, and B. Chance, "A novel approach to optical tomography," *Bioimaging* **1**, 40–46 (1993), pp. 35–64.
11. E. B. de Haller, "Time-resolved transillumination and optical tomography," *J. Biomed. Opt.* **1**, 7–17 (1996).
12. J. C. Hebden, S. R. Arridge, and D. T. Depty, "Optical imaging in medicine: I. Experimental techniques," *Phys. Med. Biol.* **42**, 825–840 (1997); S. R. Arridge and J. C. Hebden, "Optical imaging in medicine: II. Modelling and reconstruction," *Phys. Med. Biol.* **42**, 841–853 (1997).
13. E. Marshall, "Search for a killer: focus shifts from fat to hormones in a special report on breast cancer," *Science* **259**, 618–621 (1993).
14. R. R. Alfano, A. Pradhan, G. C. Tang, and S. J. Wahl, "Optical spectroscopic diagnosis of cancer and normal breast tissues," *J. Opt. Soc. Am. B* **6**, 1015–1023 (1989).
15. M. S. Feld, R. Manoharan, J. Salenius, J. Ornstein-Carndona, T. J. Romer, J. F. Brennan III, R. R. Dasari, and Y. Wang, "Detection and characterization of human tissue lesions with near-infrared Raman spectroscopy," in *Advances in Fluorescence Sensing Technology II*, J. R. Lakowicz, ed., Proc. SPIE **2388**, 99–104 (1995).
16. K. M. Yoo and R. R. Alfano, "Time-resolved coherent and incoherent components of forward light scattering in random media," *Opt. Lett.* **15**, 320–322 (1990). For a discussion of the characteristics of photons transmitted through a turbid medium, see Refs. 1 and 12 and relevant references in those papers.
17. W. Cai, B. B. Das, F. Liu, M. Zevallos, M. Lax, and R. R. Alfano, "Time-resolved optical diffusion tomographic image reconstruction in highly scattering turbid media," *Proc. Natl. Acad. Sci. USA* **93**, 13561–13564 (1996).
18. W. Cai, B. B. Das, F. Liu, Fan An Zeng, M. Lax, and R. R. Alfano, "Three-dimensional image reconstruction in highly scattering turbid media," in *Proceedings of Optical Tomography and Spectroscopy of Tissue: Theory, Instrumentation, Model, and Human Studies II*, B. Chance and R. R. Alfano, eds., Proc. SPIE **2979**, 241–248 (1997).
19. J. Singer, F. Grunbaum, P. Kohn, and J. Zubelli, "Image reconstruction of the interior of the bodies that diffuse radiation," *Science* **248**, 990–992 (1990).
20. H. Jiang, K. D. Paulsen, U. L. Osterberg, B. W. Pogue, and M. S. Patterson, "Optical image reconstruction using frequency-domain data: simulations and experiments," *J. Opt. Soc. Am. A* **13**, 253–266 (1996).
21. S. B. Colak, D. G. Papaioannou, G. W. 't Hooft, M. B. van der Mark, H. Schomberg, J. C. J. Paasschens, J. B. M. Melissen, and N. A. A. J. van Asten, "Tomographic image reconstruction from optical projections in light-diffusing media," *Appl. Opt.* **36**, 180–213 (1997).
22. A. H. Hielscher, A. Klose, D. Catarious, Jr., and K. Hanson, "Tomographic imaging of biological tissue by time-resolved model-based iterative image reconstruction," in *Advances in Optical Imaging and Photon Migration*, J. G. Fujimoto and M. S. Patterson, eds., Vol. 21 of 1998 OSA Trends in Optics and Photonics (1998), pp. 156–161.
23. H. Jiang "Three-dimensional optical image reconstruction: finite element approach," in *Advances in Optical Imaging and Photon Migration*, J. G. Fujimoto and M. S. Patterson, eds., Vol. 21 of 1998 OSA Trends in Optics and Photonics (1998), pp. 168–170.
24. C. L. Matson, N. Clark, L. McMackin, and J. S. Fender, "Three-dimensional tumor localization in thick tissue with the use of diffuse photon-density waves," *Appl. Opt.* **36**, 214–220 (1997).
25. S. R. Arridge and W. R. B. Lionheart, "Nonuniqueness in diffusion-based optical tomography," *Opt. Lett.* **23**, 882–884 (1998).
26. P. C. Hansen, "Analysis of discrete ill-posed problems by means of the L curve," *SIAM (Soc. Ind. Appl. Math.) Rev.* **34**, 561–580 (1992).
27. H. J. van Staveren, C. J. M. Moes, J. van Marle, S. A. Prahl, and M. J. van Gemert, "Light scattering in Intralipid-10% in the wavelength range of 400–1100 nm," *Appl. Opt.* **30**, 4507–4514 (1991).
28. Q. Fu, F. Seier, S. K. Gayen, and R. R. Alfano, "High-average-power, kilohertz-repetition-rate, sub-100-fs Ti:sapphire amplifier system," *Opt. Lett.* **22**, 712–714 (1997).
29. M. A. O'Leary, D. A. Boas, B. Chance, and A. G. Yodh, "Simultaneous scattering and absorption images of heterogeneous media using diffusive waves within the Rytov approximation," in *Proceedings of Optical Tomography and Spectroscopy of Tissue: Theory, Instrumentation, Model, and Human Studies II*, B. Chance and R. R. Alfano, eds., Proc. SPIE **2979**, 320–327 (1997).
30. S. K. Gayen, M. E. Zevallos, M. Alrubaiee, J. M. Evans, and R. R. Alfano, "Two-dimensional near-infrared transillumination imaging of biomedical media with a chromium-doped forsterite laser," *Appl. Opt.* **37**, 5327–5336 (1998).